

Analysis of the $S_2 \leftarrow S_0$ vibronic spectrum of the ortho-cyanophenol dimer using a multimode vibronic coupling approach

Sabine Kopec, Philipp Ottiger, Samuel Leutwyler, and Horst Köppel

Citation: *The Journal of Chemical Physics* **142**, 084308 (2015); doi: 10.1063/1.4913363

View online: <http://dx.doi.org/10.1063/1.4913363>

View Table of Contents: <http://scitation.aip.org/content/aip/journal/jcp/142/8?ver=pdfcov>

Published by the AIP Publishing

Articles you may be interested in

Excitonic splitting and vibronic coupling in 1,2-diphenoxyethane: Conformation-specific effects in the weak coupling limit

J. Chem. Phys. **138**, 204313 (2013); 10.1063/1.4807300

The S_1/S_2 exciton interaction in 2-pyridone-6-methyl-2-pyridone: Davydov splitting, vibronic coupling, and vibronic quenching

J. Chem. Phys. **135**, 154311 (2011); 10.1063/1.3652759

S_1/S_2 excitonic splittings and vibronic coupling in the excited state of the jet-cooled 2-aminopyridine dimer

J. Chem. Phys. **131**, 204308 (2009); 10.1063/1.3266937

S_1-S_0 vibronic spectra of benzene clusters revisited. II. The trimer

J. Chem. Phys. **117**, 3675 (2002); 10.1063/1.1494977

Coupling of a Jahn–Teller pseudorotation with a hindered internal rotation in an isolated molecule: 9-hydroxytriptycene

J. Chem. Phys. **109**, 10767 (1998); 10.1063/1.477775



Analysis of the $S_2 \leftarrow S_0$ vibronic spectrum of the *ortho*-cyanophenol dimer using a multimode vibronic coupling approach

Sabine Kopec,¹ Philipp Ottiger,² Samuel Leutwyler,² and Horst Köppel¹

¹Physikalisch-Chemisches Institut, Universität Heidelberg, Im Neuenheimer Feld 229, D-69120 Heidelberg, Germany

²Departement für Chemie und Biochemie, Universität Bern, Freiestrasse 3, CH-3012 Bern, Switzerland

(Received 11 December 2014; accepted 10 February 2015; published online 26 February 2015)

The $S_2 \leftarrow S_0$ vibronic spectrum of the *ortho*-cyanophenol dimer (oCP)₂ is analyzed in a joint experimental and theoretical investigation. Vibronic excitation energies up to 750 cm⁻¹ are covered, which extends our previous analysis of the quenching of the excitonic splitting in this and related species [Kopec *et al.*, J. Chem. Phys. **137**, 184312 (2012)]. As we demonstrate, this necessitates an extension of the coupling model. Accordingly, we compute the potential energy surfaces of the *ortho*-cyanophenol dimer (oCP)₂ along all relevant normal modes using the approximate second-order coupled cluster method RI-CC2 and extract the corresponding coupling constants using the linear and quadratic vibronic coupling scheme. These serve as the basis to calculate the vibronic spectrum. The theoretical results are found to be in good agreement with the experimental highly resolved resonant two-photon ionization spectrum. This allows to interpret key features of the excitonic and vibronic interactions in terms of nodal patterns of the underlying vibronic wave functions. © 2015 AIP Publishing LLC. [<http://dx.doi.org/10.1063/1.4913363>]

I. INTRODUCTION

Hydrogen-bonded molecular dimers represent a relevant class of excitonically coupled aggregates which are important constituents of very different systems such as conjugated polymers, molecular crystals, and photobiological complexes.^{1–5} These dimers offer the advantage of being representative for larger systems but are still small enough to allow detailed experimental and theoretical investigations. These help to unravel the underlying microscopic mechanisms responsible for their properties of interest. In one of our groups, efforts have been undertaken for more than a decade to exploit this feature and study the excitonic energy splittings and vibrational excitations accompanying the $S_2/S_1 \leftarrow S_0$ electronic transition in such systems using resonant-two photon-ionization (R2PI) spectra. The examples chosen were typically doubly H-bonded aromatic and heteroaromatic species, most notably the 2-aminopyridine (2AP)₂, *ortho*-cyanophenol (oCP)₂, 2-pyridone (2PY)₂, and related molecular dimers.^{6–11} The systems all show similar excitonic splitting schemes, with a (mostly) forbidden $S_1 \leftarrow S_0$ transition, that becomes slightly allowed upon asymmetric isotopic substitution.

More recently, we have focussed on the interplay between excitonic and vibronic couplings and have shown this to have a drastic impact on the magnitude of the excitonic energy splittings, reducing them by a factor of 10–40 compared to the purely electronic (Davydov) splittings.^{7,12,13} This “quenching of the excitonic splitting” has been obtained based on a combination of model Hamiltonians well-known in excitonic coupling theory^{14–16} and modern *ab initio* calculations for all the relevant vibronic coupling constants entering the

description. Very satisfactory agreement with the observed S_1/S_2 energy splittings could be obtained,^{6,7,12} thus reconciling the large discrepancy between *ab initio* theory and experiment that existed before.⁸ We have adopted and compared two different approaches using Förster perturbation theory and an effective mode *ansatz* that yielded a complementary description of the phenomenon.^{12,13} We furthermore analysed the quenching in terms of a nonadiabatic tunneling splitting on the lower adiabatic potential energy surface (PES). This interpretation has been adopted by other groups.^{17,18}

In the present work, we augment the range and scope of the analysis presented in Refs. 7 and 12. While earlier mostly the origins of the $S_1 \leftarrow S_0$ and/or $S_2 \leftarrow S_0$ electronic transition have been considered, we now address the spectral energy range up to typically 300–700 cm⁻¹ excitation energy and elucidate the importance of the vibronic couplings from a more general perspective. Not surprisingly, this more extended scope of investigation necessitates more advanced theoretical approaches. Whereas earlier the traditional Fulton-Gouterman (FG) Hamiltonian^{14,15} and Förster perturbation theory¹⁶ have been used and found appropriate, these turn out to be not sufficiently accurate for our present purposes, see below. Therefore, we rely instead on the more general so-called linear vibronic coupling (LVC) approach¹⁹ which has proven successful in a wide range of applications that are not primarily related to excitonic coupling systems.^{20,21} As prominent examples, we mention the successful analysis of complex spectral structures in the photoelectron and absorption spectra of systems ranging from triatomics such as NO₂ (Ref. 22) and SO₂ (Ref. 23) to the benzene cation and its fluoro derivatives.^{24,25} From the systematic point of view, the phenomenon of vibronic intensity borrowing could be treated

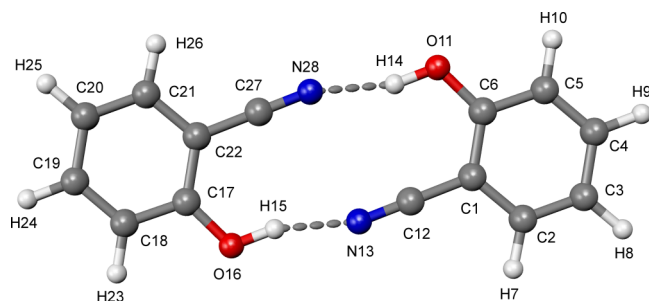


FIG. 1. Optimized ground state geometry of (oCP)₂ (RI-CC2/aug-cc-pVTZ) with atom labels.

on an equal footing with strong non-Born-Oppenheimer effects.^{19–21} All these aspects will be seen to play a role also for the present investigation. Although the basic methodological ingredients like Taylor series expansion and diabatic electronic states are similar, in the FG approach and in the LVC approach, the latter naturally allows to relax certain constraints between coupling constants which exist within the FG formalism. Moreover, and more importantly, it offers a natural framework for including also the *intermonomer* vibrational modes in the description. These are often important and have already been introduced in a more *ad hoc*⁷ or a specialized^{26,27} manner. The LVC approach is used here for the dimer as a whole, and thus the intermonomer modes enter the description naturally.

As a representative example, we focus on the *ortho*-cyanophenol dimer (oCP)₂, see Fig. 1. The monomers are bound by two antiparallel O–H···N hydrogen bonds to form a centrosymmetric (*C*_{2h}) dimer. Since the oCP chromophore has a planar geometry in the ground and excited states of both the monomer and dimer, this simplifies the theoretical investigations of the vibronic spectrum. In the energy range from 32 850 to 33 600 cm^{−1}, the spectrum is dominated by the presence of the *S*₁ (*A*_g) and *S*₂ (*B*_u) excited electronic states. Only the *S*₂ ← *S*₀ transition is dipole-allowed while the *S*₁ ← *S*₀ transition is forbidden by dipole selection rules in *C*_{2h}. We compare our theoretical results for this energy range to the experimental R2PI spectrum that has been measured in one of our groups. The (oCP)₂ system has been investigated previously by Zehnacker-Rentien *et al.*²⁸ They performed quantum chemical calculations at the density functional level with the B3LYP functional using the cc-pVTZ basis and discussed fluorescence excitation and dispersed fluorescence as well as ground state IR spectra. Our previous comparison of experimental and calculated, quenched excitonic splittings for (oCP)₂ showed a good agreement within ≈20%.¹²

This contribution is organized as follows: Sec. II starts with a short summary of the Fulton-Gouterman model, followed by an introduction to the general vibronic coupling treatment and an overview of the dynamical methods employed for this work. In Sec. III, we outline the computational details of the quantum chemical as well as dynamical calculations and describe the experimental techniques employed. Results for the optimized geometries, coupling constants, and spectra are presented in Sec. IV. The conclusions are given in Sec. V.

II. THEORETICAL FRAMEWORK

A. Fulton-Gouterman model

Vibronic coupling in molecular homodimers is often described by a model Hamiltonian originally introduced by Witkowski and Moffitt²⁹ and subsequently elaborated (and simplified) by Fulton and Gouterman.^{14,15} Following frequent use in the literature, we refer to this Hamiltonian as FG model below. Here, the nuclear vibrational motion is given by identical harmonic oscillators in each monomer *A, B* with frequency ω , normal mode coordinates Q_A and Q_B , and linear coupling l occurring upon electronic excitation. The coupling parameters for both monomers are equal, since the monomers are taken to be identical. The electronic excitonic coupling V_{AB} is assumed to be independent of the nuclear coordinate. The corresponding Hamiltonian for the simplified case of a single pair of modes is given by^{14,15,30}

$$\mathcal{H}_{FG} = \left(E_{exc} + \frac{P_A^2}{2\mu} + \frac{\mu\omega^2}{2} Q_A^2 + \frac{P_B^2}{2\mu} + \frac{\mu\omega^2}{2} Q_B^2 \right) \mathbf{1} + \begin{pmatrix} lQ_A & V_{AB} \\ V_{AB} & lQ_B \end{pmatrix}, \quad (1)$$

where $\mathbf{1}$ is the unit matrix and E_{exc} is the vertical excitation energy in the monomer.

Transformation to a delocalized electronic and vibrational basis, where the latter is denoted by $Q_{\pm} = \sqrt{\mu\omega/2\hbar}(Q_A \pm Q_B)$, and introducing the reduced linear coupling parameter $b = l\sqrt{\hbar/2\mu\omega}$ yields

$$\mathcal{H}_{deloc} = \frac{1}{\sqrt{2}} \begin{pmatrix} 1 & 1 \\ 1 & -1 \end{pmatrix} \mathcal{H}_{FG} \frac{1}{\sqrt{2}} \begin{pmatrix} 1 & 1 \\ 1 & -1 \end{pmatrix} \quad (2)$$

$$= \left(E_{exc} + \frac{\hbar\omega}{2} (P_+^2 + Q_+^2 + P_-^2 + Q_-^2) \right) \mathbf{1} + \begin{pmatrix} V_{AB} + bQ_+ & bQ_- \\ bQ_- & -V_{AB} + bQ_+ \end{pmatrix}. \quad (3)$$

Due to the simple approximations embodied in the FG model, the coupling constants for both Q_+ and Q_- are identical. Furthermore, the FG model in its original sense only accounts for intramonomer modes. For a more detailed description, we refer to the original publications^{14,15} or to our recent work.^{7,12,13}

B. General vibronic coupling model

1. Hamiltonian

In the present work, we study the structure of the vibronic spectrum of (oCP)₂ in the framework of a multimode vibronic coupling model as described, for example, in Ref. 19. Like in Eqs. (1) and (3), the Hamiltonian relies on a diabatic electronic basis where the nuclear kinetic energy operator T_N is diagonal and the coupling matrix \mathbf{W} arises from the potential energy part

$$\mathcal{H} = T_N \mathbf{1} + \mathbf{W}(\mathbf{Q}). \quad (4)$$

The elements of \mathbf{W} in Eq. (4) are given in terms of dimensionless normal coordinates Q and are expanded in a

Taylor series around a chosen reference geometry $Q_0 = 0$ which is taken as the ground state equilibrium geometry of the dimer. Truncation of the expansion after the first and second order terms leads to the linear and quadratic vibronic coupling models (LVC and QVC, respectively).¹⁹

The LVC Hamiltonian reads¹⁹

$$\mathbf{W}^{(1)}(Q_g, Q_u) = V_0(Q_g, Q_u)\mathbf{1} + \begin{pmatrix} E_1 + \sum_i k_i^{(1)} Q_{gi} & \sum_j \lambda_j Q_{uj} \\ \sum_j \lambda_j Q_{uj} & E_2 + \sum_i k_i^{(2)} Q_{gi} \end{pmatrix}, \quad (5)$$

with the ground state potentials $V_0(Q_g, Q_u) = \sum_{i,j} \frac{\hbar\omega_{gi}}{2} Q_{gi}^2 + \frac{\hbar\omega_{uj}}{2} Q_{uj}^2$.

Only symmetry selection rules are used to provide restrictions on the coupling constants and on the vibrational modes which are relevant to the diagonal and off-diagonal elements of the coupling matrix.¹⁹ For $\mathbf{W}^{(1)}$, they read

$$\Gamma_1 \otimes \Gamma_Q \otimes \Gamma_2 \supset \Gamma_{Ag}. \quad (6)$$

Equation (6) states that a vibrational mode with symmetry Γ_Q can couple electronic states with symmetries Γ_1 and Γ_2 only if their direct product comprises the totally symmetric irreducible representation Γ_{Ag} of the point group of the molecule. Therefore, the totally symmetric modes g always lead to intrastate couplings with elements in the diagonal of the coupling matrix \mathbf{W} whereas the off-diagonal elements (index u , interstate couplings) depend on the symmetry of the system in question. The corresponding modes are referred to as coupling modes and are normally different (for $\Gamma_1 \neq \Gamma_2$) from the totally symmetric modes appearing in the diagonal of \mathbf{W} . The coupling modes cause a repulsion of the PES, and for large interstate coupling constants this leads to a double-well shape of the lower electronic surface along the respective (non-totally symmetric) normal mode coordinate. The totally symmetric modes, called tuning modes, modulate the energy separation between the coupled electronic states.¹⁹

For brevity, the extension to quadratic coupling terms is only given for a single coupling mode Q_u and a single tuning mode Q_g ,

$$\mathbf{W}(Q_g, Q_u) = V_0(Q_g, Q_u)\mathbf{1} + \begin{pmatrix} E_1 + k^{(1)}Q_g + \frac{1}{2}\gamma_g^{(1)}Q_g^2 + \frac{1}{2}\gamma_u^{(1)}Q_u^2 & \lambda Q_u + \frac{1}{2}\mu_{gu}Q_g Q_u \\ \lambda Q_u + \frac{1}{2}\mu_{gu}Q_g Q_u & E_2 + k^{(2)}Q_g + \frac{1}{2}\gamma_g^{(2)}Q_g^2 + \frac{1}{2}\gamma_u^{(2)}Q_u^2 \end{pmatrix}, \quad (7)$$

with γ_g and γ_u as quadratic coupling constants and μ_{gu} as the mixed quadratic coupling.

2. Vibronic eigenfunctions

Vibronic eigenfunctions for interacting PESs involve products of an electronic and a vibrational factor (it is only due to integration over the electronic coordinates that the Hamiltonian of Eq. (4) appears as a matrix in electronic function space and the eigenfunctions as vectors in the same space). Without that integration, the vibronic eigenfunctions for two coupled states generally appear as

$$\Psi(\mathbf{r}, \mathbf{Q}) = \phi_1(\mathbf{r})\chi_1(\mathbf{Q}) + \phi_2(\mathbf{r})\chi_2(\mathbf{Q}). \quad (8)$$

In the presence of a symmetry and for two vibrational modes as in Eq. (7), this expression reads more explicitly,

$$\Psi_{A_g}(\mathbf{r}, Q_g, Q_u) = \phi_{A_g}(\mathbf{r})\chi_g(Q_g, Q_u) + \phi_{B_u}(\mathbf{r})\chi_u(Q_g, Q_u), \quad (9)$$

$$\Psi_{B_u}(\mathbf{r}, Q_g, Q_u) = \phi_{A_g}(\mathbf{r})\chi_u(Q_g, Q_u) + \phi_{B_u}(\mathbf{r})\chi_g(Q_g, Q_u). \quad (10)$$

For later reference, we have already introduced the symmetry labels A_g and B_u appropriate to the point group C_{2h} of (oCP)₂. The labels g and u (gerade and ungerade) denote the symmetry of the vibrational wave function (WF) χ under the sign change operation of the non-totally symmetric coordinate Q_u only, see Eq. (7). In a power series expansion, this implies that the $\chi_g(Q_g, Q_u)/\chi_u(Q_g, Q_u)$ contain only even/odd powers of the coupling mode coordinate Q_u .

3. Adiabatic potential energy surfaces

The adiabatic PESs are generally obtained by diagonalization of the diabatic coupling matrix $\mathbf{W}(\mathbf{Q})$ of Eq. (4), i.e., taking the nuclear coordinates as parameters. For the specific case of Eq. (7), we get

$$V_{1,2}(Q_g) = \frac{\hbar\omega_g}{2}Q_g^2 + \frac{\gamma^{(1,2)}}{2}Q_g^2 + k^{(1,2)}Q_g + E_{1,2}, \quad (11)$$

$$V_{1,2}(Q_u) = \frac{\hbar\omega_u}{2}Q_u^2 + \frac{E_1 + E_2}{2} + \frac{\gamma_u^{(1)} + \gamma_u^{(2)}}{4}Q_u^2 \pm \sqrt{\left(\frac{E_2 - E_1}{2} + \frac{\gamma_u^{(2)} - \gamma_u^{(1)}}{4}Q_u^2\right)^2 + (\lambda Q_u)^2}, \quad (12)$$

where we have put the other coordinate (Q_u or Q_g) to zero for simplicity. Equations (11) and (12) immediately show how the linear and quadratic coupling constants can be determined from the adiabatic PES. For the totally symmetric modes, the intrastate linear coupling constant for the state i is¹⁹

$$k_i = \left. \frac{\partial V_i(Q)}{\partial Q_g} \right|_{Q=0} \quad (i = 1, 2). \quad (13)$$

From the difference of the adiabatic PES, one obtains the interstate coupling constant

$$\lambda = \sqrt{\frac{1}{8} \frac{\partial^2 (V_2 - V_1)^2}{\partial Q_u^2}} \Big|_{Q=0}. \quad (14)$$

For sufficiently large coupling constants λ , the PESs along the coupling modes show the aforementioned double-minimum structure. This effect is intensified in the multi-mode case.¹⁹ For $\Delta < L$, the corresponding stabilization energy upon symmetry lowering through the coupling modes is given by

$$E_{stab} = \frac{(\Delta - L)^2}{2L}, \quad \text{with } L = \sum_i \frac{\lambda_i^2}{\hbar\omega_i} \quad \text{and } \Delta = \frac{E_2 - E_1}{2}. \quad (15)$$

Note that, even in the linear coupling approximation ($\gamma = \mu = 0$), the Hamiltonian of Eq. (7) generalizes the FG-Hamiltonian widely used in the literature to treat excitonically coupled systems.^{19,31–34} This is easily seen from the delocalized FG Hamiltonian of Eq. (3). This transformed Hamiltonian shows the analogy between the FG and the general LVC model, where the relation between the coupling parameters is $\lambda = k^{(1)} = k^{(2)} = b$, $\omega_g = \omega_u$.

C. Dynamical calculations

In quantum dynamical calculations, vibronic spectra are often obtained via wave-packet propagation. The spectral intensity distribution $P(E)$ is thereby calculated as the Fourier transform of the autocorrelation function $C(t)$,

$$P(E) \propto \int e^{iEt} C(t) dt, \quad \text{with } C(t) = \langle \Psi(0) | \Psi(t) \rangle. \quad (16)$$

$C(t)$ is also known as the survival amplitude, that is, a measure for the probability that the wave function at time t is equal to the initial wave function $\Psi(t=0)$. The wave-packet propagation is done using the powerful multiconfigurational time-dependent Hartree (MCTDH) method developed in the Heidelberg group.^{35–37} The basis of this method is the use of a multiconfigurational wave function that is a weighted sum over Hartree products of optimized time-dependent basis functions φ for each degree of freedom f ,

$$\Psi(Q_1, \dots, Q_f, t) = \sum_{j_1=1}^{n_1} \cdots \sum_{j_f=1}^{n_f} A_{j_1 \dots j_f}(t) \varphi_{j_1}^{(1)}(Q_1, t) \cdots \varphi_{j_f}^{(f)}(Q_f, t). \quad (17)$$

The latter are expanded in a primitive basis set. To increase the computational efficiency, several degrees of freedom are combined (mode combination) and treated as a single particle, thus increasing to the so-called MCTDH contraction effect. Equations of motions for the expansion coefficients and single-particle functions are derived through the Dirac-Frenkel variational principle.^{35–37}

III. COMPUTATIONAL AND EXPERIMENTAL METHODS

A. Computational details

In its electronic ground state, the oCP dimer has a planar equilibrium structure corresponding to the C_{2h} symmetry group (see also below). Its 78 vibrational degrees of freedom

TABLE I. Number of primitive basis functions (PBFs) as well as of time-dependent single-particle functions (SPF) used in the MCTDH calculation. The vibrational modes (degrees of freedom, DOF) combined to particles are given in the first column. The second column denotes the number of primitive harmonic oscillator functions for each DOF. The numbers of SPFs are listed in column three.

Modes	PBF basis	SPF basis
(ν_4, ν_5)	20, 28	19
ν_7	20	8
(ν_9, ν_{10})	18, 15	12
ν_{13}	13	4
(ν_{17}, ν_{18})	20, 18	10
ν_{24}	10	2

transform as follows:

$$\Gamma_Q = 27a_g \oplus 26b_u \oplus 13a_u \oplus 12b_g. \quad (18)$$

As a first step in the investigation, geometry optimizations for the ground and first two excited singlet states were carried out. This was followed by frequency calculations, where the harmonic frequencies were obtained numerically.

The adiabatic PESs for the S_0 , S_1 , and S_2 states were determined by single-point calculations at normal mode displacements $Q_i = \pm 0.5, \pm 1.0, \pm 2.0$, and ± 3.0 for a given mode. The linear and quadratic vibronic coupling constants were obtained by least squares fits to the electronic excitation energies (see below for more details). All electronic structure calculations of (oCP)₂ were performed at the RI-CC2/aug-cc-pVTZ level, of the oCP monomer at the RI-CC2/cc-pVTZ level, both employing the TURBOMOLE program package Version 6.0.³⁸

The vibronic spectra were computed using the MCTDH program suite.³⁹ The propagation calculations were performed using a basis of single-particle-functions and a product of harmonic oscillator functions as initial wave function. The basis set details used in the subsequent calculation are given in Table I. The contraction effect caused by the shorter length of the single-particle vector compared to the number of primitive basis functions is $\approx 10^6$. The line spectra for the 2-mode cases reported in Sec. IV D were obtained using the Lanczos algorithm as implemented in the MCTDH package.³⁹ The corresponding vibronic eigenfunctions for the 2-mode case are accessible through relaxation calculations using so-called single-set block-improved relaxation.⁴⁰ The adiabatic spectra shown for comparison were generated with the aid of the POTFIT routine^{41,42} available in the MCTDH package.

B. Experimental techniques

The experimental setup has been discussed in detail previously.^{6,9} The vibrationally cold oCP complexes were synthesized in a supersonic jet-expansion. The oCP sample (Aldrich, 99%) was placed in a home-built, magnetically actuated nozzle and heated to 80 °C. Neon was used as a carrier gas with a backing pressure of 1.2 bars. The skimmed molecular beam was overlapped spatially and temporally with an excitation and an ionization laser in the source of a 1 m time-of-flight mass spectrometer. Molecular ions were

produced according to the R2PI scheme where the complexes are excited from the vibrationally cold electronic ground state to the vibrational levels of an electronically excited state that is accessible by one-photon excitation and are subsequently ionized by a second laser pulse at 228 nm. The resulting, singly charged ions were detected using a microchannel plate detector (MCP).

The output of a Radiant-Dyes NarrowScan dye laser (Sulforhodamine B), pumped by the 532 nm output of a Nd:YAG laser was used for excitation ($\sim 50 \mu\text{J}/\text{pulse}$, UV-bandwidth $\sim 0.09 \text{ cm}^{-1}$). The spectra were calibrated by measuring the fundamental frequency with a HighFinesse Angstrom WS6 high precision wavemeter. The 228 nm ionization laser pulses ($200 \mu\text{J}$) were produced by sum-frequency mixing of the 640 nm output of a dye-laser (DCM), pumped by the 532 nm output of an Nd:YAG laser, with the 355 nm output of the same pump laser. Nozzle and lasers were operated at a repetition rate of 20 Hz.

IV. RESULTS AND DISCUSSION

A. Equilibrium geometries and vibrational analysis

The optimized ground state structure and the atom numbering scheme are shown in Fig. 1. The S_1 and S_2 excited electronic states transform as A_g and B_u , respectively, in the C_{2h} point group. With calculated vertical excitation energies of $35\,693 \text{ cm}^{-1}$ and $36\,001 \text{ cm}^{-1}$ (see Table II), they are separated by only 308 cm^{-1} and are therefore subject to vibronic coupling. This gives rise to the LVC scheme adopted in Eq. (5), the coupling and tuning modes being of b_u and a_g symmetry.

A list of bond lengths and angles of the S_0 equilibrium structure, the S_1 state structure both at the C_{2h} symmetry-restricted (first order) saddle point and at its C_s symmetric equilibrium geometry, and the S_2 state at its C_{2h} symmetric structure is given in the supplementary material (Tables SI and SII).⁴³

For comparison, the monomer structure parameters are included to the supplementary material as well (Table SIII).⁴³ It is seen there that upon dimerization, the intramonomeric hydrogen bond becomes wider, while the intermonomeric hydrogen bond is formed. The dimerization does not have an effect on the CH bond lengths, and only a very minor one on the aromatic CC bond lengths and the angles not located at the functional groups. Due to the dimeric hydrogen bonds, the angle at the hydroxy group $\angle \text{H14-O11-C6}$ is widened from the typical 109.2° to 114.9° , while the cyano-angle $\angle \text{C1-C12-N13}$ is widened by 5.5° to be almost linear in the dimer. Therefore, the intramonomeric hydrogen bond H14-N13 becomes 0.35 \AA longer, i.e., it virtually disappears

in the dimer. These changes also have small effects on the neighboring bond lengths and angles.

Tables SI and SII⁴³ also give evidence of the geometrical changes occurring upon electronic excitation. Upon a C_{2h} restricted geometry optimization in the S_1 state, the intermolecular hydrogen-bond is shortened by 0.135 \AA . The aromatic bond lengths are all slightly increased, while there is no effect on the corresponding angles. Only the lengths and angles at the two functional groups show deviations up to 0.03 \AA and 2.2° . The equilibrium structure of the second excited state is similar to this despite a somewhat shorter (by $\approx 0.015 \text{ \AA}$) hydrogen bond. Full relaxation in the S_1 state leads to the loss of the equivalence of the two monomers resulting in a C_s symmetric structure. Apart from minor deviations, the C_{2h} restricted S_1 structure is the average of those of the left and right monomers in the dimeric C_s structure.

A complete list of all dimer normal modes is given in the supplementary material, Table SIV.⁴³ The numbering of the modes follows the ground state vibrational frequency in ascending order, irrespective of symmetries. The same holds for the monomer modes. For a complete list of a' monomer modes, see Ref. 13 (supplementary material).

We show the displacement vectors for a selected set of in-plane monomer and dimer modes in Figs. 2 and 3. The comparison of monomer modes (Fig. 2) with dimer modes (Fig. 3) shows similarities and differences in the relation between monomer and dimer vibrations. From model considerations, the dimer modes are expected to be positive and negative linear combinations of monomer modes, differing only by a few wavenumbers in energy. This is true, for example, for the in-plane dimer modes ν_{17} and ν_{18} that have their origin in ν_7^{mono} . This mode-pair also occurs in the 2-aminopyridine dimer and has been previously discussed in detail.⁷ Another pair of dimer modes is ν_9 and ν_{10} . Here, ν_9 is a negative combination of ν_1^{mono} , with an energy difference of 41.1 cm^{-1} . However, ν_{10} clearly shows admixing of a rotational

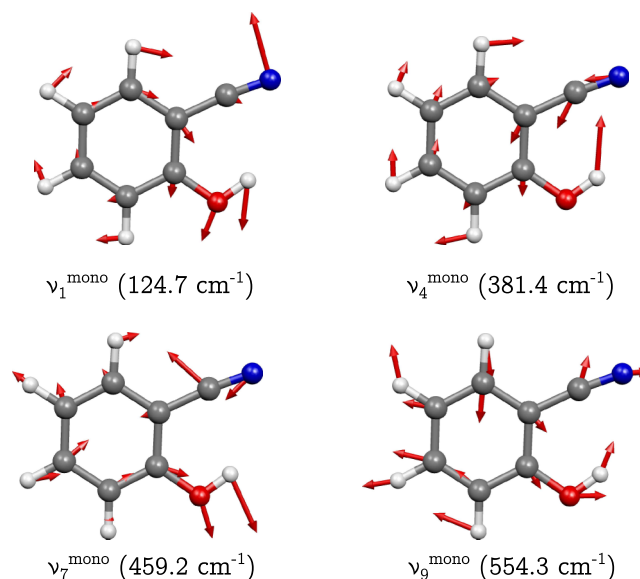


FIG. 2. Displacement vectors for the lowest-frequency totally symmetric (a') *o*-cyanophenol monomer modes.

TABLE II. Vertical and adiabatic S_1 and S_2 excitation energies of $(\text{oCP})_2$ at the RI-CC2/aug-cc-pVTZ level (in cm^{-1}).

	$S_1 (C_s)$	$S_1 (C_{2h})$	$S_2 (C_{2h})$
vertical	-	35 693	36 001
adiabatic	33 846	34 575	35 003

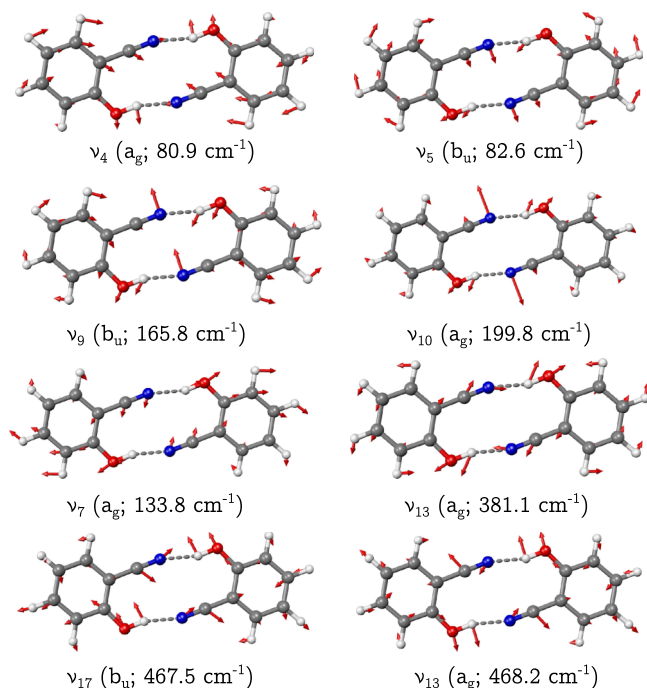


FIG. 3. Displacement vectors for some important low-frequency in-plane (a_g , b_u) (*o*-cyanophenol)₂ dimer modes.

motion, since the displacement vectors at the benzyl ring are significantly smaller than for ν_1^{mono} . The frequency shift of 74.8 cm^{-1} supports this observation. The deviation between monomer and dimer modes is most pronounced for modes that involve a stretching or bending of the hydrogen bond. A different example for the latter is the mode pair ν_{31} , ν_{32} (b_g , a_u) that represents an out-of-plane CCOH torsional motion with a frequency of about 740 cm^{-1} . The corresponding a'' monomeric mode ν_6^{mono} has a frequency of only 447 cm^{-1} .

The intermonomeric modes ($\nu_1 - \nu_5$ and ν_7) play a special role. They have very low frequencies, between 10 and 150 cm^{-1} , and are composed of monomer translations and rotations. Of these, only the mode pair ν_4 , ν_5 (H-bond shearing and cogwheel) with frequencies of 80.9 and 82.5 cm^{-1} and mode ν_7 (H-bond stretch with admixture of rotation, 133 cm^{-1}) have the proper a_g and b_u symmetries to enter the LVC description for the S_1 and S_2 excited states. We will show later that these are the most important modes for the analysis of the vibronic spectrum.

B. Determination and discussion of coupling parameters of (oCP)₂

The monomer coupling parameters were taken from Ref. 12. There they were obtained by least squares fits to the excited state PES using the shifted harmonic oscillator model. Only the S_1 state of oCP was considered, since the energy difference to the second excited state is 1.26 eV and the Born-Oppenheimer separation is expected to be valid. The coupling parameters for modes with frequencies up to 800 cm^{-1} are collected in Table III.

The dimer coupling constants have been obtained by least squares fits of the QVC model to the *ab initio* calculated

TABLE III. Coupling parameters of the totally symmetric oCP monomer vibrational modes (RI-CC2/cc-pVTZ) up to 800 cm^{-1} , obtained by harmonic least squares fits to the PESs. Parameters are taken from Ref. 13. All modes included in the calculation of the spectrum are marked with an asterisk.

Mode	$\omega_{GS} (\text{cm}^{-1})$	$b (\text{cm}^{-1})$	$b^2/\omega_{GS} (\text{cm}^{-1})$	b^2/ω_{GS}^2
1*	124.7	92.7	68.9	0.552
4*	381.4	-105.5	29.2	0.077
7*	459.2	-350.3	267.2	0.582
9*	554.3	-47.4	4.0	0.007
11	591.6	151.7	38.9	0.066
13	730.2	268.3	98.6	0.135

adiabatic PESs (see Eqs. (11) and (12)). For the totally symmetric modes in the framework of linear (quadratic) couplings, the PESs are shifted harmonic oscillators (including a frequency change).

Anharmonicity along single-mode coordinates in the ground state of hydrogen-bonded systems is a well-known phenomenon and has been the subject of extensive studies.⁴⁴ As an example, for the (oCP)₂ system, Fig. 4(a) shows the ground state potentials along the totally symmetric normal mode ν_{10} including the harmonic ground state potential and the anharmonic fit to the *ab initio* single-point energies calculated along Q_{10} . The harmonic model is clearly not in good agreement with the *ab initio* energies. To analyse the impact of the ground state anharmonicity on the excited state PESs, we compare the coupling constants resulting from harmonic fits to the excitation energies with those resulting from harmonic fits to the PESs. For mode ν_{10} , the first one is depicted in Fig. 4(b) and is of very satisfactory quality. The second fit is shown as a dotted line in Fig. 4(c). The solid line in Fig. 4(c) is obtained by adding the anharmonic fit to the ground state potential from Fig. 4(a) and the harmonic fit to the excitation energy from Fig. 4(b). The comparison of the solid and dotted lines in Fig. 4(c) clearly demonstrates that the fully harmonic fit does not well reproduce the excited state PES. For mode ν_{10} , e.g., the values for the linear coupling constant in the first excited state in the two approaches are 45.3 cm^{-1} and 91.4 cm^{-1} . This leads to a difference in the Huang-Rhys factor (also called Poisson parameter in the literature) $S = k^2/2\omega^2$ of a factor of 4. Therefore, the vibrational excitation is negligible in one case and clearly visible in the other. For all modes considered, the fit to the excitation energy nicely confirms the quadratic vibronic coupling model. The anharmonic character of the PES of the S_1 and S_2 excited states is “inherited” from the ground state.

Since the experimental spectrum is of high resolution and also the observed quenched excitonic splitting is rather small, very small inaccuracies in the coupling constants have a rather large impact on the quality of the theoretical results. Therefore, we obtained all coupling constants through least squares fits to the excitation energies rather than to the PESs to eliminate the ground state anharmonicity from the fit. The corresponding coupling constants for the a_g modes up to 800 cm^{-1} are compiled in Table IV. Therein, the frequency ω_{GS} is the RI-CC2 harmonic frequency. For both excited states, k is the linear and γ the quadratic vibronic coupling constant

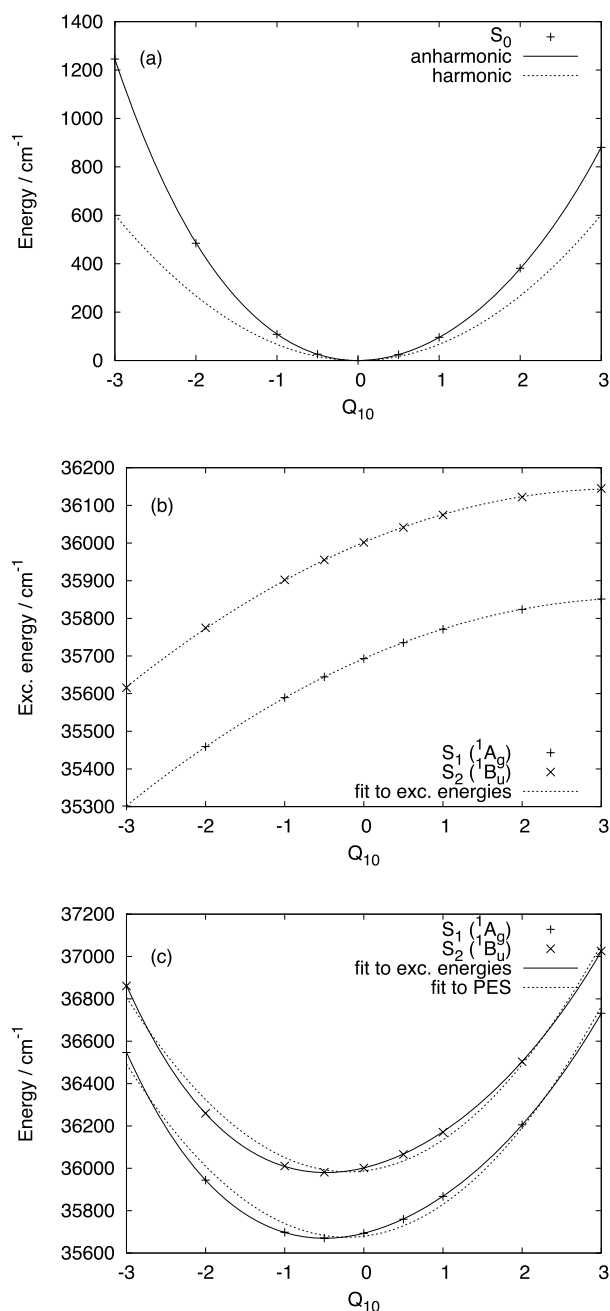


FIG. 4. Determination of coupling constants for mode ν_{10} (a_g). (a) Comparison between anharmonic and harmonic ground state potentials. The energy at the ground state equilibrium geometry ($Q = 0$) is set to zero. (b) QVC fit to the excitation energies. The negative curvatures indicate a frequency lowering upon excitation. (c) Comparison between different QVC fits to the excited state PES. The dashed line gives the results when fitting directly to the PES of the excited state, the solid line results from fitting to the excitation energy of the central panel. In the latter case, the plotted data are obtained by adding the anharmonic ground state potential of panel (a).

obtained through least squares fits; the first corresponds to a shift relative to the ground state potential minimum and the latter to a frequency change in the electronically excited state. The sum of the harmonic ground state frequency and the quadratic coupling constant γ therefore is an approximation to the excited-state frequency. Additionally, the Huang-Rhys factor for each mode is given. The modes that are explicitly treated in the subsequent calculation of the spectra are marked

with an asterisk. Fig. 5 shows the agreement between the *ab initio* data and the fit to the excitation energies along these modes (ν_4 , ν_7 , ν_{13} , and ν_{18}). The negative curvatures are due to a frequency lowering upon excitation (i.e., negative values of γ).

For the 1D-cuts along the b_u coupling modes, a least squares fit to the squared difference of the interacting surfaces yields the linear interstate coupling constant λ as well as the difference in the quadratic coupling constants (see Eq. (12)). The sum of the quadratic coupling constants is determined from the sum of the excitation energies. The values obtained are collected in Table V for modes with frequencies up to 800 cm^{-1} . Besides the harmonic ground state frequency ω_{GS} , the linear and the quadratic coupling constants γ for both excited states (obtained from both the difference and the sum of the excitation energies) are given, together with the Huang-Rhys factor for each mode. The modes that are explicitly considered in the subsequent calculation of the spectra are marked with an asterisk. Fig. 6 displays the least squares fit functions to the sum (solid) and difference (dotted) of the excitation energies along these modes (ν_5 , ν_9 , and ν_{17}). For graphical reasons, the difference is given as a negative quantity. The negative curvature of the sum of the excitation energies indicates a frequency lowering. The fits of the model are seen to be in good agreement with the *ab initio* data.

Key energetic quantities for the first two excited states are given in Table II. It lists the vertical excitation energies for the S_1 and S_2 excited states and compares them with energies obtained under C_{2h} -constrained and fully relaxed structural optimizations. The energy gain due to the geometry relaxation in the S_1 state of 1847 cm^{-1} ($=35693 \text{ cm}^{-1} - 33846 \text{ cm}^{-1}$) can be decomposed into the C_{2h} symmetry-constrained structural relaxation ($1118 \text{ cm}^{-1} = 35693 \text{ cm}^{-1} - 34575 \text{ cm}^{-1}$) and the asymmetric in-plane distortion ($729 \text{ cm}^{-1} = 34575 \text{ cm}^{-1} - 33846 \text{ cm}^{-1}$). In earlier work,¹³ we related these findings to the FG model and found for the C_{2h} -constrained structural relaxation 1281 cm^{-1} and for the asymmetric distortion a stabilization energy of 1131 cm^{-1} . The deviations are approximately 15% and 35%, respectively.¹³ We are now able to compare with the predictions of the present coupling model. The structural relaxation can be assigned to the a_g modes in the S_1 -state, in which the energy gain amounts to 1064 cm^{-1} . The symmetry-lowering through coupling modes is given by the stabilization energy in the multi-mode case (see Eq. (15)) and amounts to $E_{stab} = 729 \text{ cm}^{-1}$. The results obtained using the linear vibronic coupling model are in excellent agreement with the full (i.e., model-independent) *ab initio* calculations.

For the quantum dynamical analysis discussed below, only the most relevant modes are included in the vibronic Hamiltonian. These are determined by their frequencies and the size of the Huang-Rhys factor. However, from our previous work,^{7,12,13} it is clear that all vibrational modes contribute to quenching the energy gap between the excited states. To account for this feature, we introduce a “prequenched” excitonic splitting as an effective energy difference between the two coupled surfaces. This is taken to represent the vibronic quenching by the higher-frequency modes, not included below, and is in some cases chosen

TABLE IV. Coupling parameters of the totally symmetric (oCP)₂ modes (RI-CC2/aug-cc-pVTZ) up to 800 cm⁻¹, obtained by least squares fits to the excitation energies. All modes included in the calculation of the spectrum are marked with an asterisk.

Mode	ω_{GS} (cm ⁻¹)	$k^{(1)}$ (cm ⁻¹)	$k^{(2)}$ (cm ⁻¹)	$\gamma^{(1)}$ (cm ⁻¹)	$\gamma^{(2)}$ (cm ⁻¹)	$(k^{(1)})^2/2\omega_{GS}^2$	$(k^{(2)})^2/2\omega_{GS}^2$
4*	80.9	-67.4	-50.0	-33.8	-32.5	0.347	0.191
7*	133.8	127.4	85.2	-20.2	-16.2	0.453	0.203
10*	199.5	91.4	87.6	-25.9	-27.0	0.105	0.096
13*	381.1	-170.7	-152.4	-21.8	-22.6	0.100	0.080
18*	468.2	371.4	362.6	-26.7	-27.4	0.315	0.300
24*	570.1	153.9	148.7	-31.6	-34.8	0.036	0.034
25	594.4	107.0	104.7	-9.3	-10.3	0.016	0.016
30	729.8	-267.0	-270.1	-33.9	-35.8	0.067	0.068

phenomenologically such that the computed, quenched excitonic splitting, obtained as the difference between the first lines in the calculated S_1 and S_2 spectra, well approximates the experimentally observed splitting. The prequenching only has a minor impact on the shape of the spectrum but leads to an enormous difference in the final quenched excitonic splitting. Moreover, we will see in Sec. V that the prequenching splitting can be well estimated from the treatments of Refs. 12 and 13.

C. Analysis of spectra

The experimental spectrum has been measured up to 750 cm⁻¹ above the S_2 vibronic origin. Also the computed spectrum has been restricted to this region. The experimental spectrum is dominated by the $S_2(^1B_u) \leftarrow S_0(^1A_g)$ transition

and its associated a_g vibrational excitations, which are fully allowed. As will be shown below, vibrational b_u excitations of the $S_1(^1A_g)$ state also become allowed via vibronic coupling.

1. Fulton-Gouterman model

As a starting point, we compare the calculated spectrum based on the FG model with the experimental 2C-R2PI spectrum in Fig. 7. Diagonalization of the original FG Hamiltonian (Eq. (1)) yields the spectra for both locally excited states. For comparison with the experimental spectrum, restriction to the symmetry-allowed $S_2 \leftarrow S_0$ transition is achieved by employing the FG Hamiltonian in the electronically and vibrationally delocalized basis (see Eq. (3)). Therefore, in the spectrum, the modes appear as positive

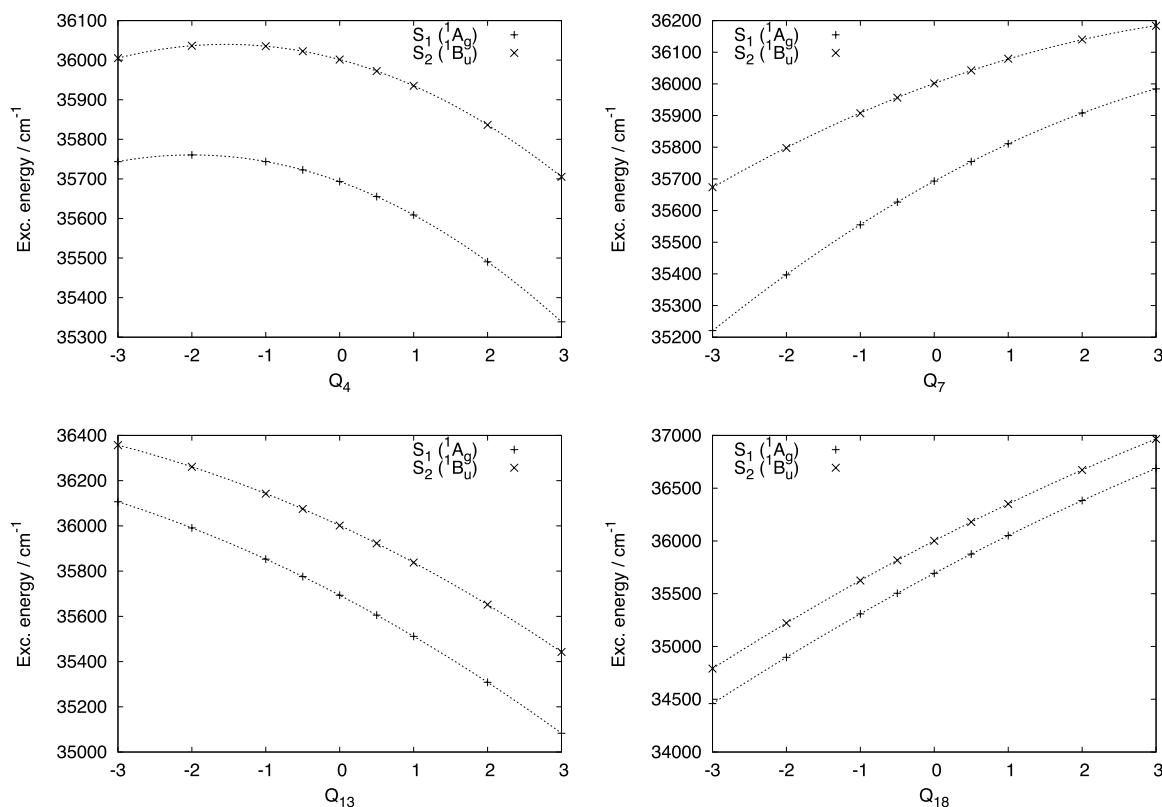


FIG. 5. Least squares fits (dashed lines) to the excitation energies of the $S_1(^1A_g)$ and $S_2(^1B_u)$ excited states along the a_g modes 4, 7, 13, and 18. + and x display the *ab initio* data points.

TABLE V. Coupling parameters of the b_u -symmetric (oCP)₂ modes (RI-CC2/aug-cc-pVTZ) up to 800 cm⁻¹, obtained by least squares fits to the sum and difference of the excitation energies (compare Eq. (12)). All modes included in the calculation of the spectrum are marked with an asterisk.

Mode	ω_{GS} (cm ⁻¹)	$\gamma^{(1)}$ (cm ⁻¹)	$\gamma^{(2)}$ (cm ⁻¹)	λ (cm ⁻¹)	$\lambda^2/2\omega_{GS}^2$
5*	82.6	-36.5	-36.5	71.1	0.370
9*	165.8	-50.4	-21.5	67.8	0.084
16	407.0	-25.3	-25.3	12.5	5×10^{-4}
17*	467.5	-35.6	-24.2	373.5	0.319
23	559.2	-28.9	-28.9	80.2	0.010
26	596.0	-8.8	-8.8	150.5	0.032
29	724.3	-37.7	-37.7	216.2	0.045

and negative combinations Q_+ and Q_- of the monomeric modes. The vibrations considered for the calculation are the four lowest-frequency totally symmetric modes of the oCP-monomer (ν_1^{mono} , ν_4^{mono} , ν_7^{mono} , ν_9^{mono} , see Table III and Fig. 2) in the energy range up to 560 cm⁻¹. To account for the effect of the higher-frequency modes, we introduce a prequenched excitonic splitting of 69.5 cm⁻¹. The corresponding quenching (or reduction) factor Γ is determined in a non-phenomenological way by applying Förster's perturbation theory expression¹⁶ $\Gamma = \prod_i \exp -b_i^2/(\hbar\omega_i)^2$ to all the higher-frequency modes starting from mode ν_{11}^{mono} . For more details, we refer to Ref. 13 from which also the coupling constants are taken. The spectra are shifted to a common origin.

In the calculated FG spectrum of Fig. 7(b), the line at 117 cm⁻¹ represents an excited state with a roughly equal mixture of one and two quanta of the monomer mode ν_1^{mono} in

its negative linear combination, i.e., levels 1_-^1 and 1_-^2 . In line with the symmetry considerations of Sec. II B 2, the former (latter) component is associated with the A_g (B_u) symmetric electronic wave function. The following line at 125 cm⁻¹ corresponds to a single-quantum excitation of the positive linear combination of ν_1^{mono} (1_+^1). The three lines at 235, 242, and 250 cm⁻¹ are higher quanta of mode ν_1^{mono} , namely, 1_-^3 , $1_+^1 1_-^2$, and 1_+^2 . Even a third series of lines is visible at 363 cm⁻¹, namely, $1_+^1 1_-^3$, $1_+^2 1_-^2$, and 1_-^4 . Note that lines with an even number of quanta in 1_- are always associated with the B_u -symmetric electronic wave function (as already stated above), whereas odd quanta come with the A_g -symmetric electronic wave function. Somewhat separated is the first excitation of mode ν_4^{mono} at 382 cm⁻¹, with a rather small relative intensity of 0.04, reflecting the small Huang-Rhys factor of 0.08. The excitations of mode ν_7^{mono} follow at 454 and 459 cm⁻¹, also as a single quantum 7_+^1 and one or two quanta 7_-^1 and 7_-^2 . This is

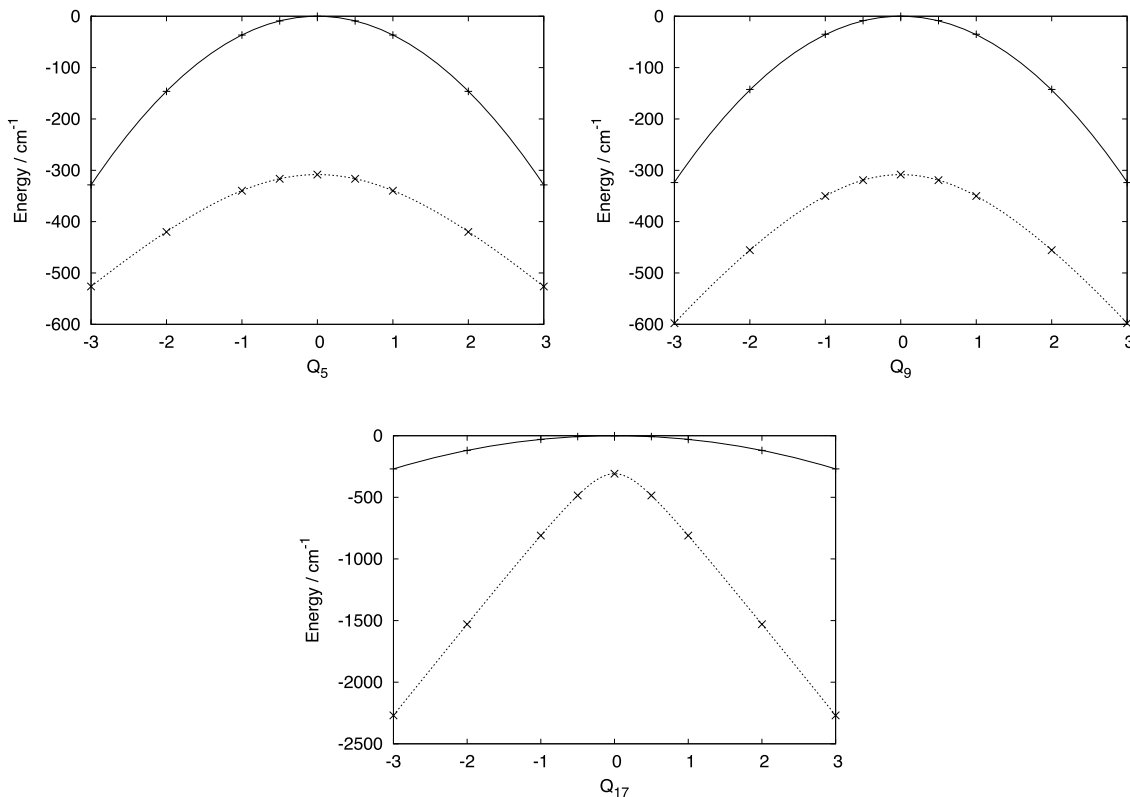


FIG. 6. Least squares fit to the sum (solid) and difference (dashed) of the excitation energies along b_u modes 5, 9, and 17. The sum at $Q = 0$ is set to zero. + and x display the sum and the difference of the *ab initio* calculated energies (in cm⁻¹) of the S_1 and S_2 states, respectively.

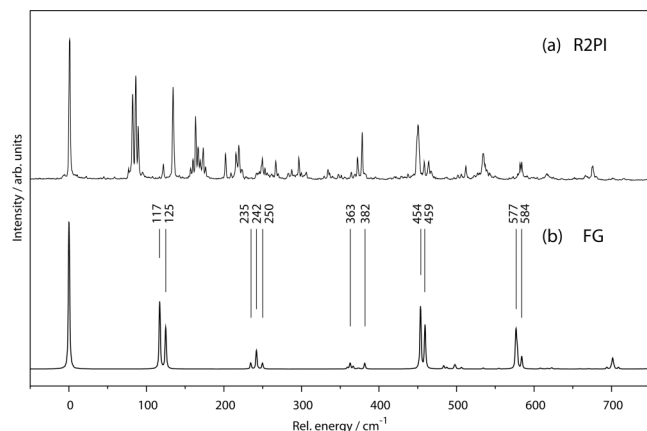


FIG. 7. Comparison of the experimental R2PI spectrum (a) with a 4-mode spectrum (b) calculated in the framework of the Fulton-Gouterman model, employing only monomer vibrational modes. In panel (b), the labels of several weaker lines have been omitted for clarity.

again similar to mode ν_1^{mono} . More details will be discussed in Sec. IV D. The combined excitations of ν_1^{mono} and ν_7^{mono} are seen at 577 and 584 cm⁻¹. All assignments of the calculated FG spectrum are summarized in Table VI.

The experimental and theoretical spectra are in acceptable agreement for the energy range of mode ν_7^{mono} . This is due to the similarity of ν_7^{mono} with the corresponding dimer modes ν_{17} and ν_{18} (see Sec. IV A). The FG model is sufficient in this case. The deviations between theory and experiment are most obvious in the low-frequency range. The dimer vibrations ν_9 and ν_{10} that correspond to the monomer mode ν_1^{mono} are 40 to 75 cm⁻¹ higher in energy and the lines are therefore expected to be shifted to higher energy (see Fig. 8). Instead, the experimental spectrum shows the excitation of low-frequency intermonomeric modes at about 80 cm⁻¹, which are not accounted for in the FG spectrum due to the limitation of the model.

In previous related work on the 2-aminopyridine dimer, the FG model has been extended in an *ad hoc* way by including also intermonomer modes with empirically fitted values of the coupling constants.⁷ Here, we aim for a more rigorous approach with parameters computed *ab initio*

TABLE VI. Assignment of spectral features of the $S_2 \leftarrow S_0$ transition of the *ortho*-cyanophenol dimer calculated within the FG approach, see Fig. 7. All frequencies in cm⁻¹.

Mode	FG
1_2^-	117
1_+^1	125
1_3^3	235
$1_+^1 1_2^-$	242
1_+^2	250
$1_+^2 1_2^-$	363
4_+^1	382
7_2^-	454
7_+^1	459
$1^1 7^1$	577
$1^1 7^1$	584

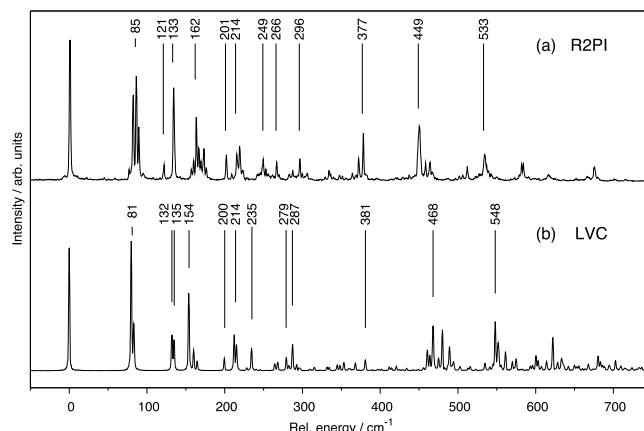


FIG. 8. Comparison of the experimental R2PI spectrum (a) with a 9-mode spectrum (b) calculated in the framework of the LVC model.

and therefore proceed by using a more general vibronic Hamiltonian (Eq. (5)) for the analysis of the spectrum.

2. Linear vibronic coupling scheme

Fig. 8 shows a comparison between the experimental R2PI spectrum and the calculated 9-mode LVC spectrum. Both spectra are shifted to a common origin. The 2C-R2PI spectrum of (oCP)₂ is measured over the 32 850–33 600 cm⁻¹ range. The first band in the experimental spectrum in Fig. 8(a) is assigned to the 0_0^0 band, which lies at 32 855 cm⁻¹. The vibronic Hamiltonian comprises the a_g -symmetric modes ν_4 , ν_7 , ν_{10} , ν_{13} , ν_{18} , and ν_{24} , as well as the b_u -symmetric modes ν_5 , ν_9 , and ν_{17} . Their frequencies are all in the energy range of interest. The coupling constants are taken from Tables IV and V. The phenomenological, prequenched excitonic splitting used is 105.8 cm⁻¹, see also Sec. V.

All assignments of the experimental and calculated spectra are summarized in Table VII. For the LVC spectrum, they are based on energetic considerations, together with the calculated nodal properties of the vibronic levels, computed as indicated in Sec. III A.

TABLE VII. Comparison of experimental (R2PI) and theoretical (LVC) spectral features of the $S_2 \leftarrow S_0$ transition (see Fig. 8) of (oCP)₂. All frequencies in cm⁻¹.

Mode	R2PI	LVC
ν_4^1	85.3	{79.8, 83.2}
ν_5^2	121.2	132.1
ν_7^1	133.4	134.8
ν_4^2	162.5	153.8
ν_{10}^1	201.2	199.5
$\nu_4^1 \nu_7^1$	{214.4, 218.2}	{212.2, 215.0}
ν_4^3	-	234.5
$\nu_4^1 \nu_{10}^1$	266.0	279.3
$\nu_4^2 \nu_7^1$	295.8	287.3
ν_{13}^1	377.4	380.9
ν_{18}^1	449.3	468.0
$\nu_4^1 \nu_{18}^1$	533.4	548.0

The first detail that stands out in the computed spectrum, Fig. 8(b), in comparison to the FG spectrum in Fig. 7(b) is the pair of low-frequency lines near 80 cm^{-1} . They correspond to the intermonomeric mode ν_4 (H-bond shearing, see Fig. 3). The experimental spectrum shows a band multiplet, while the LVC spectrum shows a doublet of lines with similar intensity. For further discussion of the calculated doublet structure, we refer to Sec. IV D. In the following, we address possible explanations for the experimentally observed multiplet structure.

From comparative calculations including the low-frequency b_g symmetric mode ν_3 (40.4 cm^{-1}), we consider it unlikely that a double excitation of mode ν_3 (within the QVC scheme) is responsible for one of these extra lines. Also the inclusion of quadratic couplings in modes ν_4 or ν_5 as well as their mixed coupling does not result in further lines in this region of the spectrum. We suspect that the experimentally observed multiplet is due to couplings of vibrations ν_4 and ν_5 with the very low-frequency modes ν_1 , ν_2 , and ν_3 that appear between 10 and 50 cm^{-1} , see the list of frequencies (Table SIV in the supplementary material.⁴³) As an indication, we point out that also all higher quanta of mode ν_4 show a similar multiplet structure. These putative couplings have not been analyzed in detail, since the methods employed in this work rely on rectilinear Cartesian displacement coordinates that are not suited for the description of the out-of-plane low-frequency modes ν_1 , ν_2 , and ν_3 .

The line at 135 cm^{-1} can be assigned to the totally symmetric intermonomeric mode ν_7 (see Fig. 3). The experimental spectrum shows a line at 121 cm^{-1} that does not appear in the LVC spectrum. Due to symmetry constraints, we can exclude an excitation of the b_g -symmetric mode ν_6 (calculated at 121.6 cm^{-1}). Instead, we assign it as the double excitation of mode ν_5 , which appears as the line at 132 cm^{-1} in the calculated spectrum. A series of lines for the double excitation of mode ν_4 appears at 154 cm^{-1} about 8 cm^{-1} lower than in the experimental spectrum. The following lines in the LVC spectrum (Fig. 8(b)) can be assigned to mode ν_{10} (200 cm^{-1}), a combination of modes ν_4 and ν_7 (214 cm^{-1}) and a triple excitation of mode ν_4 (235 cm^{-1}). We further assign the line at 279 cm^{-1} to a combined excitation of modes ν_4 and ν_{10} and that at 287 cm^{-1} to a combined excitation of two quanta in mode ν_4 and one quantum in mode ν_7 . The corresponding lines in the experimental spectrum occur at 266 cm^{-1} and at 296 cm^{-1} .

The intensity of the a_g mode ν_{13} at 381 cm^{-1} is significantly underestimated by the LVC model. Since its ground state PES shows a harmonic behaviour and the quadratic fit to the excitation energies works well (see Fig. 5), the deviations cannot be caused by anharmonicity. Also the inclusion of quadratic coupling parameters for mode ν_{13} does not improve the relative intensity (see Table IV). The small intensity is therefore probably due to an underestimation of the linear coupling along this mode by the *ab initio* calculation. At 468 cm^{-1} appears the excitation of mode ν_{18} . The shift relative to experiment is 19 cm^{-1} . The higher-frequency region in the experimental spectrum shows combined excitations of mode ν_{18} with either mode ν_4 or mode ν_7 . Here, the assignment in the calculated spectrum is not unique.

Despite some deviations, the spectra are in good overall agreement. We recall that all frequencies and coupling constants are computed purely *ab initio* without any empirical adjustment. Clearly, the results obtained using the LVC model are superior to the FG model.

D. Assignment of low-dimensional spectra and wave functions

For a more detailed insight into the vibronic coupling phenomenon, we analyze a two-mode spectrum including only the two low-frequency intermonomeric vibrations ν_4 (a_g) and ν_5 (b_u), see Fig. 3. As before, we introduce a phenomenological, prequenched splitting between the electronically excited states. Due to the suppression of more modes than in the spectrum of Fig. 8, the prequenched excitonic splitting is reduced to 40 cm^{-1} . The spectra are shown in Fig. 9 together with the numbering of the vibronic lines. The blue (upward) lines belong to states of B_u vibronic symmetry (symmetry-allowed transitions), while the red (downward) lines indicate A_g vibronic symmetry (forbidden transitions; not relevant for comparing with experiment, but included for the discussion). Due to the reduced dimensionality of the calculations, the spectral range is reduced to 200 cm^{-1} . The first line in the B_u spectrum is set to zero energy. We present the vibronic WFs corresponding to the vibronic levels according to their symmetry as contour lines employing a colouring scheme to indicate their sign. They are collected in Fig. 10 for the states that appear in the A_g spectrum and Fig. 11 for those in the B_u spectrum. The left columns contain the electronic part of the WF corresponding to the lower A_g -symmetric (S_1) electronic state, whereas the right columns show the B_u -symmetric (S_2) electronic WF component, see also Eq. (10). In accordance with symmetry considerations, the A_g -symmetric electronic WF component for the A_g -symmetric vibronic lines shows an even number of nodes in the coupling mode ν_5 , whereas for the B_u -symmetric electronic WF component, the number of nodes is odd (see

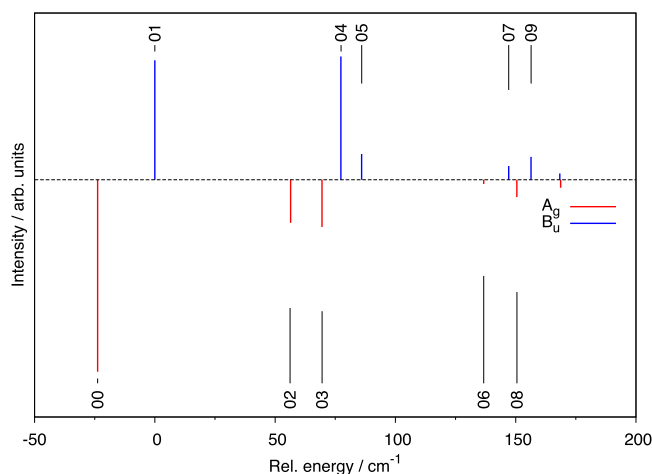


FIG. 9. LVC model 2-mode spectrum of A_g (red, downward) and B_u (blue, upward) vibronic symmetry corresponding to Fig. 8. Only Q_4 and Q_5 are retained with an effective, prequenched energy gap of 40 cm^{-1} . The associated excited-state vibronic wave functions are shown in Figs. 10 and 11.

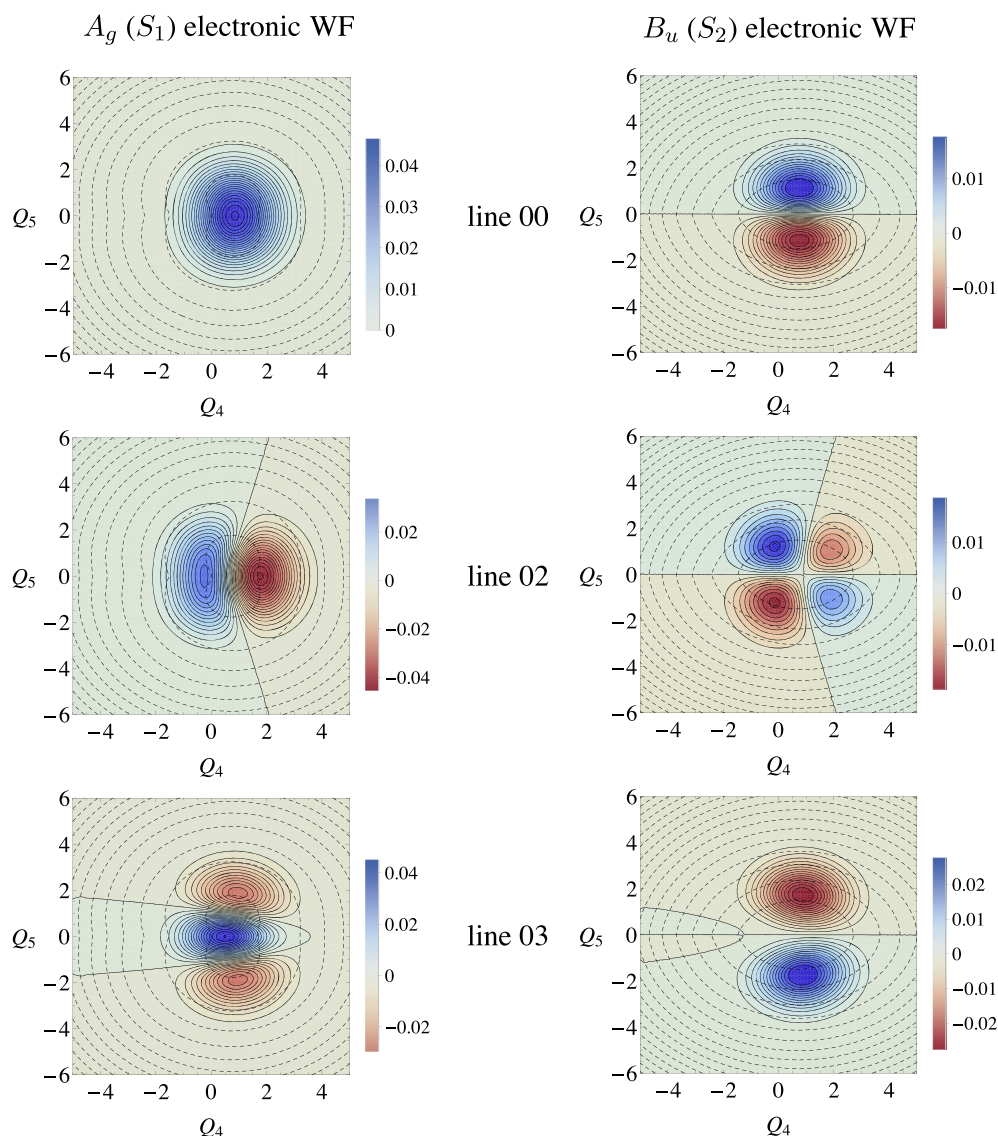


FIG. 10. Wave functions (solid, colored lines) and potential energy surfaces (dashed lines) for A_g vibronic symmetry states of the 2-mode spectrum (red, downward in Fig. 9, forbidden transitions). The different wave function amplitude scales to the right of each sub-figure reflect the different weights of the electronic wave function as listed in Table VIII.

Fig. 10). For the B_u vibronic states, even and odd nodes are interchanged (see Fig. 11). All subfigures of Fig. 10 and Fig. 11 include the adiabatic PESs for the S_1 and S_2 states as dashed contour lines. The assignments of the vibronic lines together with the weights of the respective WFs are collected in Table VIII.

The 00 line in Fig. 9 corresponds to an excitation with a nodeless WF in the S_1 state with a contribution of 86.2%, corresponding to the optically forbidden vibronic S_1 origin. The remaining 13.8% of the vibronic WF corresponds to the fundamental of mode ν_5 in the S_2 (B_u) electronic state. The first B_u vibronic state 01 amounts to a single excitation of the intermonomeric mode ν_5 in the A_g electronic state (weight 46.1%) and a broad nodeless wave function in the B_u electronic state (53.9%). The WF components for the vibronic states 00 and 01 are interchanged relative to each other. However, state 00 clearly is the vibronic origin of the S_1 (A_g) state, whereas the contributions from the S_1 and S_2 states for 01 are almost equally mixed.

Of the following two A_g -symmetric vibronic states 02 and 03, the first consists of a fundamental excitation of mode ν_4 with a contribution of 84.4%, and a combination of single quanta of modes ν_4 and ν_5 with a contribution of 15.6%. The vibronic state 03 is a mixture of a double excitation of mode ν_5 (64.9%) with the fundamental of mode ν_5 (35.1%). Although the A_g -symmetric electronic contribution to the vibronic WF is clearly dominant, the contribution from the second excited electronic state increases with increasing vibronic energy as is seen from the weights in Table VIII. This increased mixing of the two states is expected, as the vibronic energies approach and move up in the energy range of the S_2 electronic state.

The lines 04 and 05 are symmetry-allowed (B_u) vibronic excitations of both ν_4 and ν_5 in the A_g -symmetric electronic state (40.7% and 36.8%, respectively) and are approximate mirror images of each other. The same holds for the corresponding B_u electronic components. They both appear as one node in Q_4 and a combination of zero and two nodes in Q_5

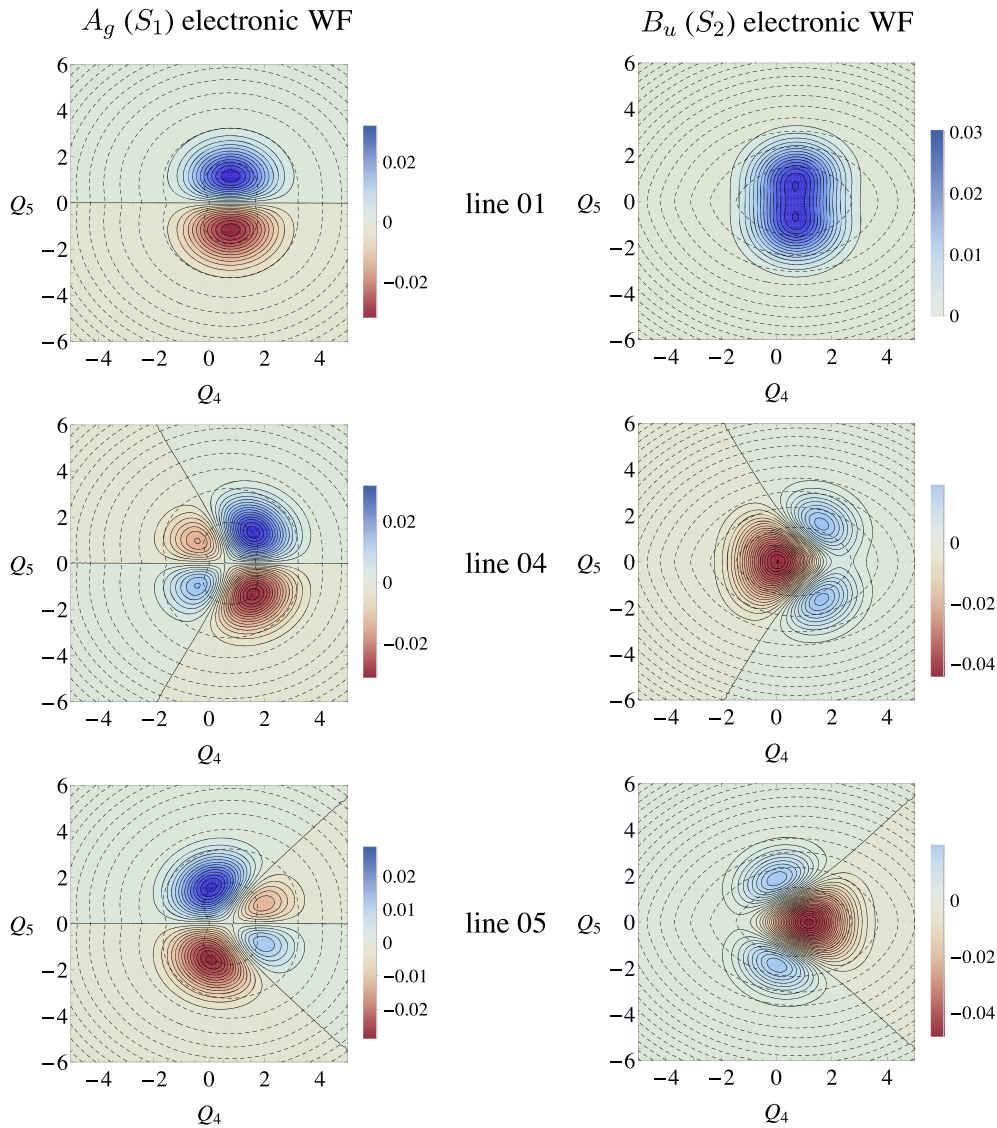


FIG. 11. Same as Fig. 10, for B_u vibronic symmetry states of the 2-mode spectrum (blue, upward in Fig. 9, allowed transitions).

(59.3% and 63.2%, respectively). The two lines are separated by 8.6 cm^{-1} . This is slightly more than the separation of 3.4 cm^{-1} for the doublet in the 9-mode LVC spectrum near 80 cm^{-1} (Fig. 8); the difference is, however, not significant. One might expect one of the lines to be the excitation of the totally symmetric mode ν_4 on the B_u electronic state, and the other one to be the excitation of the coupling mode ν_5

on the A_g electronic surface due to intensity borrowing.^{19,45} The doublet structure in both spectra is associated with the mirror images of peculiar nodal patterns displayed in Fig. 11.

For the B_u -symmetric vibronic states, the mixing of the two electronic states is in general more pronounced than for the A_g -symmetric states. Clearly, the effects observed are not solely due to intensity borrowing from the A_g -symmetric electronic state. For further insight, we neglect nonadiabatic effects and compare the LVC 2-mode spectra with spectra computed for uncoupled adiabatic PESs.¹⁹

In Fig. 12, we display the 2-mode spectra on the S_1 adiabatic surface (red, down) and the S_2 adiabatic surface (blue, up) using the same modes (ν_4 and ν_5) and parameters as for the LVC spectra of Fig. 9. The vibrational lines are denoted a, b, \dots, f for the first excited state and k, l, \dots, p for the second excited state. The corresponding six wave functions are collected in Figs. 13 and 14. In the A_g spectrum, only lines a (0.0 cm^{-1} , 0^0 origin), c (80.4 cm^{-1} , 4^1), d (109.8 cm^{-1} , 5^2), and f (160.9 cm^{-1} , 4^2) are visible. Lines

TABLE VIII. Assignment of the vibronic lines in the 2-mode spectrum of Fig. 9. Energies are given in cm^{-1} . The weights given in % refer to the electronic wave function given in the table heading.

Line	Energy	$A_g (S_1)$		$B_u (S_2)$	
00 (red)	-23.8	0_0^0	86.2%	4_{0-0}^{051}	13.8%
01 (blue)	0.0	4_{0-0}^{051}	46.1%	0_0^0	53.9%
02 (red)	56.2	4_{0-0}^{150}	84.4%	4_{0-0}^{151}	15.6%
03 (red)	69.5	4_{0-0}^{052}	64.9%	4_{0-0}^{051}	35.1%
04 (blue)	77.4	4_{0-0}^{151}	40.7%	$4_{0-0}^{150} + 4_{0-0}^{052}$	59.3%
05 (blue)	86.0	4_{0-0}^{151}	36.8%	$4_{0-0}^{150} + 4_{0-0}^{052}$	63.2%

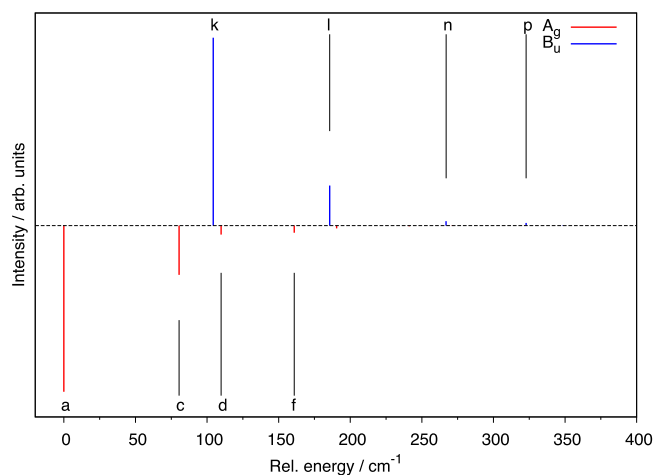


FIG. 12. Same spectrum as in Fig. 9 but recomputed in the adiabatic approximations. A_g symmetry corresponds to the lower adiabatic PES, B_u symmetry to the upper adiabatic PES. The underlying vibronic wave functions are shown in Figs. 13 and 14.

b (46.3 cm^{-1} , 5^1) and e (126.8 cm^{-1} , $4^1 5^1$) have vanishing intensity due to symmetry as they include a single excitation of the b_u -symmetric mode ν_5 . The relative energy for excitations of the a_g -symmetric mode ν_4 is as expected from the shifted

harmonic oscillator model close to the harmonic ground state frequency of 80.9 cm^{-1} . However, for the b_u -symmetric mode ν_5 , the computed adiabatic frequency is smaller by a factor of almost two, due to the repulsion of the electronically excited states, by which the lower surface is flattened.¹⁹

In the B_u spectrum, lines k (104.3 cm^{-1} , 0^0 origin), l (185.6 cm^{-1} , 4^1), n (266.9 cm^{-1} , 4^2), and p (322.8 cm^{-1} , 5^2) are visible. There, lines m (219.3 cm^{-1} , 5^1) and o (300.7 cm^{-1} , $4^1 5^1$) have vanishing intensity. Herein, the frequency for mode ν_4 again matches the harmonic ground state frequency, whereas the frequency for mode ν_5 is almost 50% larger since the upper adiabatic surface is steeper along the coupling mode.

In contrast to the coupled LVC wave functions of Figs. 10 and 11, the WF for the uncoupled adiabatic surfaces leads to regular nodal structures along both the coupling and the tuning modes. The difference between the WFs computed in the LVC scheme and the adiabatic approximation demonstrates the large amount of nonadiabaticity that is present in the (oCP)₂ system, where some of the nodal patterns result from mixing of different numbers of vibrational quanta. A similar profound difference can be found in the spectra, in particular the doublet structure of the lines at 80 cm^{-1} in Fig. 9 can be ascribed to nonadiabatic effects.

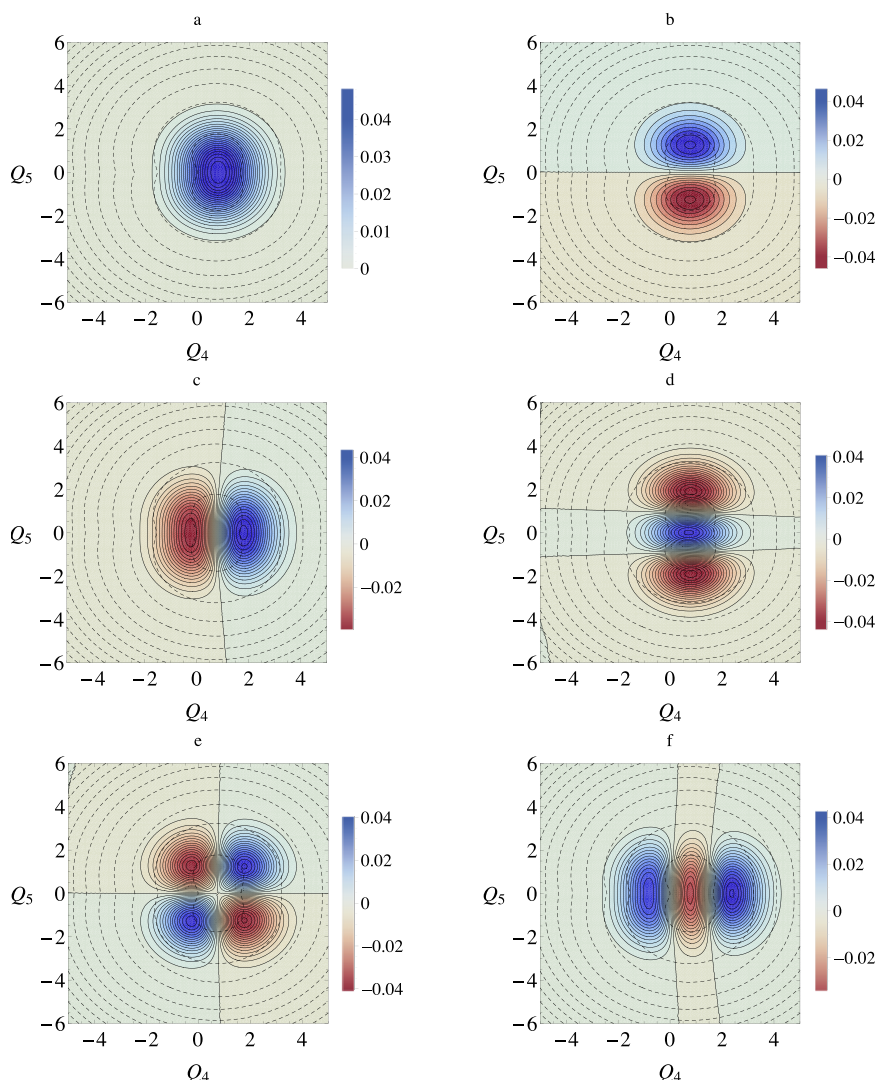


FIG. 13. Wave functions (solid, colored lines) and PESs (dashed lines) for A_g vibronic lines of the adiabatic 2-mode spectrum (red, downward in Fig. 12).

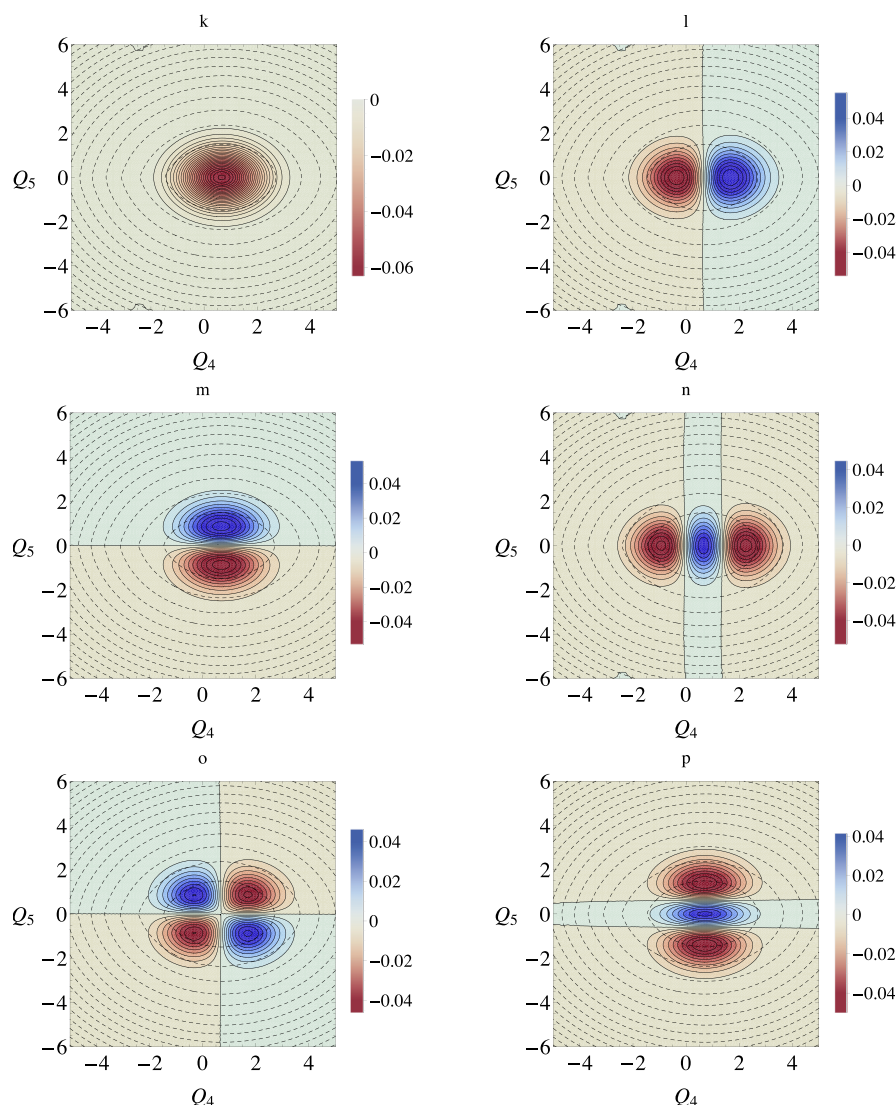


FIG. 14. Same as Fig. 10, for B_u vibronic symmetry states of the adiabatic 2-mode spectrum (blue, upward in Fig. 12).

V. CONCLUSIONS

We first show that the experimental R2PI spectrum of the *ortho*-cyanophenol dimer cannot be satisfactorily reproduced within the scope of the Fulton-Gouterman model. Instead, one has to go beyond and use more general vibronic coupling schemes. We herein presented our results for the coupled $S_1/S_2 \leftarrow S_0$ transitions of (oCP)₂ using the LVC approach and the MCTDH method. In contrast to the FG model, the spectrum is dominated by the intermonomer vibrations ν_4 , ν_5 , and ν_7 , which illustrates the limitations of the FG model. We cannot explain the multiple splittings in the low frequency mode ν_4 as well as the underestimated intensity of mode ν_{13} . However, the experimental and calculated spectra are in good overall agreement. This agreement is unprecedented for first-principles calculations like here, which rely almost exclusively on *ab initio* data for the system parameters. The present approach is relatively close to that of Nebgen *et al.*^{26,27} who use a FG type of treatment for the intramonomer modes and a quadratic coupling scheme for the intermonomer modes. This latter work differs from ours also in the amount of parameter adjustment needed to reproduce experimental spectra.

From a low-dimensional analysis of the vibronic wave functions, we identify nodal properties of the wave functions which confirm the more tentative assignments based only on energetic considerations. All vibronic states (irrespective of symmetry) involve substantial mixing of the S_1 (A_g) and S_2 (B_u) *electronic* states (taken as diabatic in accordance with the matrix Hamiltonian of Eq. (5)). For the dipole-allowed S_2 (B_u) *vibronic* symmetry, the S_2 electronic state is associated with an even number of nodes in the coupling mode coordinate, and for the S_1 electronic state, this number is odd. For the dipole-forbidden S_1 (A_g) *vibronic* symmetry, “even” and “odd” are to be interchanged. We emphasize that this qualitative feature, as well as the nodal patterns of Figs. 10 and 11, remains the same in the 9-mode calculation of Fig. 8 as in the 2-mode calculation. From comparative calculations on the uncoupled adiabatic surfaces, we can identify most of the effects observed as nonadiabatic.

Except for the prequenched (“effective”) energy gap, all system parameters are obtained from *ab initio* data without any adjustment. Even for the energy gap, we can make contact with the theoretical treatment of Refs. 12 and 13, which can be used to compute a prequenched energy gap resulting from the

coupling to all the higher-frequency modes not included in the calculation of the spectrum. For the 9-mode spectrum of Fig. 8 and the 2-mode spectrum of Fig. 9, this leads to “prequenched” gaps of 98.2 cm^{-1} and 43.9 cm^{-1} , respectively (starting from a vertical excitonic splitting of 308 cm^{-1}).⁴⁶ These numbers are close to the values actually adopted for the calculation of the spectra, namely, 105.8 cm^{-1} and 40.0 cm^{-1} according to Secs. IV C 2 and IV D. Thus, even in this respect, the phenomenological adjustment amounts to a few cm^{-1} only. Efforts are underway to further improve the treatment and understanding of the prequenching effects.

The present approach is expected to pave the way for the analysis of related systems. It should also allow for a more detailed understanding of the time-dependence of the excitation energy transfer in all these cases. Work along these lines is ongoing in our groups.

ACKNOWLEDGMENTS

It is a pleasure to dedicate this work to David R. Yarkony on the occasion of his 65th birthday. Financial support by the Deutsche Forschungsgemeinschaft under Grant No. KO945/17-1 is gratefully acknowledged. We thank the bwGRiD project⁴⁷ for the provision of computational resources. P.O. and S.L. gratefully acknowledge support from the Swiss National Science Foundation (Project No. 200020-152816).

¹*Hydrogen Bonding and Transfer in the Excited State*, 1st ed., edited by K.-L. Han and G.-J. Zhao (Wiley, Chichester, 2011), Vols. 1 and 2.

²G. D. Scholes and G. Rumbles, *Nat. Mater.* **5**, 683 (2006).

³F. C. Spano, *Annu. Rev. Phys. Chem.* **57**, 217 (2006).

⁴Y.-C. Cheng and G. R. Fleming, *Annu. Rev. Phys. Chem.* **60**, 241 (2009).

⁵C. T. Middleton, K. de La Harpe, C. Su, Y. K. Law, C. E. Crespo-Hernández, and B. Kohler, *Annu. Rev. Phys. Chem.* **60**, 217 (2009).

⁶P. Ottiger, J. A. Frey, H.-M. Frey, and S. Leutwyler, *J. Phys. Chem. A* **113**, 5280 (2009).

⁷P. Ottiger, S. Leutwyler, and H. Köppel, *J. Chem. Phys.* **131**, 204308 (2009).

⁸A. Müller, F. Talbot, and S. Leutwyler, *J. Chem. Phys.* **116**, 2836 (2002).

⁹P. Ottiger and S. Leutwyler, *J. Chem. Phys.* **137**, 204303 (2012).

¹⁰C. G. Heid, P. Ottiger, R. Leist, and S. Leutwyler, *J. Chem. Phys.* **135**, 154311 (2011).

¹¹F. A. Balmer, P. Ottiger, and S. Leutwyler, *J. Phys. Chem. A* **118**, 11253 (2014).

¹²P. Ottiger, S. Leutwyler, and H. Köppel, *J. Chem. Phys.* **136**, 174308 (2012).

¹³S. Kopec, P. Ottiger, S. Leutwyler, and H. Köppel, *J. Chem. Phys.* **137**, 184312 (2012).

¹⁴R. L. Fulton and M. Gouterman, *J. Chem. Phys.* **35**, 1059 (1961).

¹⁵R. L. Fulton and M. Gouterman, *J. Chem. Phys.* **41**, 2280 (1964).

¹⁶T. Förster, “Delocalized excitation and excitation transfer,” in *Modern Quantum Chemistry*, edited by O. Sinanoglu (Academic Press, New York, 1965), Chap. III. B, p. 93.

¹⁷E. G. Buchanan, P. S. Walsh, D. F. Plusquellic, and T. S. Zwier, *J. Chem. Phys.* **138**, 204313 (2013).

¹⁸C. König and J. Neugebauer, *J. Phys. Chem. B* **117**, 3480 (2013).

¹⁹H. Köppel, W. Domcke, and L. S. Cederbaum, *Adv. Chem. Phys.* **57**, 59 (1984).

²⁰*Conical Intersections: Electronic Structure, Dynamics and Spectroscopy*, edited by W. Domcke, D. R. Yarkony, and H. Köppel (World Scientific, Singapore, 2004).

²¹*Conical Intersections: Theory, Computation and Experiment*, edited by W. Domcke, D. R. Yarkony, and H. Köppel (World Scientific, Singapore, 2011).

²²S. Mahapatra, H. Köppel, L. S. Cederbaum, P. Stampfuss, and W. Wenzel, *Chem. Phys.* **259**, 211 (2000).

²³C. Lévesque, A. Komaianda, R. Taieb, and H. Köppel, *J. Chem. Phys.* **138**, 044320 (2013).

²⁴S. Faraji and H. Köppel, *J. Chem. Phys.* **129**, 074310 (2008).

²⁵S. Faraji, H.-D. Meyer, and H. Köppel, *J. Chem. Phys.* **129**, 074311 (2008).

²⁶B. Nebgen, F. L. Emmert III, and L. V. Slipchenko, *J. Chem. Phys.* **137**, 084112 (2012).

²⁷B. Nebgen and L. V. Slipchenko, *J. Chem. Phys.* **141**, 134119 (2014).

²⁸F. Lahmani, M. Broquier, and A. Zehnacker-Rentien, *Chem. Phys. Lett.* **354**, 337 (2002).

²⁹A. Witkowski and W. Moffitt, *J. Chem. Phys.* **33**, 872 (1960).

³⁰M. Andrzejak and P. Petelenz, *Chem. Phys.* **335**, 155 (2007).

³¹H. Köppel, “Vibronic coupling effects in spectroscopy and non-adiabatic transitions in molecular photodynamics,” in *Molecular Quantum Dynamics*, edited by F. Gatti (Springer, Heidelberg, 2014).

³²W. D. H. Köppel and L. S. Cederbaum, “The multi-mode vibronic-coupling approach,” in *Conical Intersections*, edited by D. Y. W. Domcke and H. Köppel (World Scientific, New Jersey, 2004), pp. 323–368.

³³S. Gómez-Carrasco, S. Faraji, and H. Köppel, “Multistate vibronic dynamics and multiple conical intersections,” in *Conical Intersections: Theory, Computation and Experiment* (World Scientific, Singapore, 2011), pp. 249–300.

³⁴H. Köppel and W. Domcke, “Vibronic dynamics in polyatomic molecules,” in *Encyclopedia of Computational Chemistry*, edited by P. von Ragué Schleyer (Wiley, Chichester, 1998), Vol. 5, p. 3166.

³⁵H.-D. Meyer, U. Manthe, and L. S. Cederbaum, *Chem. Phys. Lett.* **165**, 73 (1990).

³⁶M. H. Beck, A. Jäckle, G. A. Worth, and H.-D. Meyer, *Phys. Rep.* **324**, 1 (2000).

³⁷*Multidimensional Quantum Dynamics: MCTDH Theory and Applications*, edited by H.-D. Meyer, F. Gatti, and G. A. Worth (Wiley-VCH, 2009).

³⁸TURBOMOLE V6.0 2009, a development of University of Karlsruhe and Forschungszentrum Karlsruhe GmbH, 1989-2007, TURBOMOLE GmbH, since 2007, available at <http://www.turbomole.com>.

³⁹G. A. Worth, M. H. Beck, A. Jäckle, and H.-D. Meyer, The MCTDH Package, version 8.2, (2000); H.-D. Meyer, The MCTDH Package, version 8.3 (2002); The MCTDH Package, version 8.4 (2007), see <http://mctdh.uni-hd.de>.

⁴⁰H.-D. Meyer, F. L. Quéré, C. Léonard, and F. Gatti, *Chem. Phys.* **329**, 179 (2006).

⁴¹A. Jäckle and H.-D. Meyer, *J. Chem. Phys.* **104**, 7974 (1996).

⁴²A. Jäckle and H.-D. Meyer, *J. Chem. Phys.* **109**, 3772 (1998).

⁴³See supplementary material at <http://dx.doi.org/10.1063/1.4913363> for lists of bond lengths and angles for the oCP monomer and dimer as well as a complete list of frequencies of (oCP)₂.

⁴⁴B. Brauer, R. B. Gerber, M. Kabeláč, P. Hobza, J. M. Bakker, A. G. A. Riziq, and M. S. de Vries, *J. Phys. Chem. A* **109**, 6974 (2005).

⁴⁵G. Herzberg, *Electronic Spectra and Electronic Structure of Polyatomic Molecules*, reprint edition ed. (1991).

⁴⁶The prequenched gaps are obtained by applying Förster’s perturbation theory *ansatz*^{12,13,16} to the appropriate dimeric b_u modes. See Sec. II B for the relation between the FG model and the LVC scheme.

⁴⁷bwGRiD, member of the German D-Grid initiative, funded by the Ministry for Education and Research (Bundesministerium für Bildung und Forschung) and the Ministry for Science, Research and Arts Baden-Württemberg (Ministerium für Wissenschaft, Forschung und Kunst Baden-Württemberg), see <http://www.bw-grid.de>.